Electronic Supplementary Material (ESI) for Soft Matter.
This journal is © The Royal Society of Chemistry 2024

Supporting Information: Heterogeneity-induced retraction in viscoelastic fluids following cessation of flow

Patrick J. McCauley, Satish Kumar, and Michelle A. Calabrese

Department of Chemical Engineering & Materials Science

University of Minnesota, Twin Cities

SI.1 Solution of Couette flow of two adjacent UCM fluids between parallel plates

Here, the general solution for Couette flow of two adjacent UCM fluids between parallel plates at a constant applied shear rate is derived. A few key relationships between the flow variables of fluid A and B are described, which will be useful deriving an analytical solution. As stated previously, the shear stress is constant across the gap of the parallel plate geometry, and therefore:

$$\sigma_{yx,A}(y) = \sigma_{yx,B}(y) = \sigma_{yx}(y)\,, \;\; 0 \leq y \leq H \tag{SI.1.1}$$

Additionally, the velocity varies continuously across the flow geometry. Therefore, the following constraint must also be satisfied across fluid regions:

$$v_x(y=0) - v_x(y=H) = \int_{y=H}^{y=0} \frac{dv_x}{dy} dy = \int_{y=h_A}^{y=0} \frac{dv_x}{dy} dy + \int_{y=H}^{y=h_A} \frac{dv_x}{dy} dy \tag{SI.1.2}$$

with no-slip boundary conditions, $v_x(x=0) = v_w$, the imposed wall velocity driving this Couette flow, and $v_x(x=H) = 0$ at the immobile plate boundary. Because the shear rate is constant within each fluid region A and B, the derivatives $\frac{dv_x}{dy}$ may be substituted for the corresponding shear rates within each region, yielding the useful relation:

$$v_w = -\dot{\gamma}_{app} H = \int_{y=h_A}^{y=0} \dot{\gamma}_A dy + \int_{y=H}^{y=h_A} \dot{\gamma}_B dy = -\dot{\gamma}_A h_A + (-\dot{\gamma}_B) h_B \tag{SI.1.3}$$

where $\dot{\gamma}_{app} = -v_w/H$ is the applied shear rate. Note that the negative signs in front of each shear rate in equation SI.1.3 cancel out.

The analytical solution for startup and cessation of flow protocols is found by applying the stress and shear rate constraints in equations SI.1.1 and SI.1.3, respectively, to obtain an ordinary differential equation (ODE) for the stress evolution that is a function only of rheological parameters of each UCM fluid and the applied shear rate, which is constant in these protocols. First, equations

for the shear rate of fluid A and B are obtained by rearranging the following equation for the shear stress (equation 7 in the main text):

$$\tau_i \frac{d\sigma_{yx}}{dt} + \sigma_{yx} = \eta_{0,i}\dot{\gamma} \tag{SI.1.4}$$

to yield:

$$\dot{\gamma}_A = \frac{\dot{\sigma}_{yx}}{G_{0,A}} + \frac{\sigma_{yx}}{\eta_{0,A}} \tag{SI.1.5}$$

$$\dot{\gamma}_B = \frac{\dot{\sigma}_{yx}}{G_{0,B}} + \frac{\sigma_{yx}}{\eta_{0,B}} \tag{SI.1.6}$$

where the elastic modulus $G_{0,i} = \eta_{0,i}/\tau_i$ for $i = A, B$. These shear rates are substituted into the shear rate relation stated in equation SI.1.3 to obtain an equation that includes only the shear stress and its time derivative, the fluid properties, and the applied shear rate:

$$\dot{\gamma}_{app} = \frac{h_A}{H}\left(\frac{\dot{\sigma}_{yx}}{G_{0,A}} + \frac{\sigma_{yx}}{\eta_{0,A}}\right) + \frac{h_B}{H}\left(\frac{\dot{\sigma}_{yx}}{G_{0,B}} + \frac{\sigma_{yx}}{\eta_{0,B}}\right) \tag{SI.1.7}$$

where $\dot{\sigma}_{yx} = d\sigma_{yx}/dt$ denotes the time derivative of the shear stress. If similar terms are grouped, and the shear stress and its derivative are factored out, the ODE for shear stress is reduced to the following form:

$$\dot{\gamma}_{app} = \frac{\dot{\sigma}_{yx}}{G_{0,eff}} + \frac{\sigma_{yx}}{\eta_{0,eff}} \tag{SI.1.8}$$

where an effective elastic modulus and viscosity are defined as:

$$\frac{1}{G_{0,eff}} = \frac{h_A/H}{G_{0,A}} + \frac{h_B/H}{G_{0,B}} \tag{SI.1.9}$$

$$\frac{1}{\eta_{0,eff}} = \frac{h_A/H}{\eta_{0,A}} + \frac{h_B/H}{\eta_{0,B}} \tag{SI.1.10}$$

The solution to equation SI.1.8, for a constant applied shear rate, is simply:

$$\sigma_{yx}(t) = \eta_{0,eff}\dot{\gamma}_{app} + C\exp(-t/\tau_{eff}) \tag{SI.1.11}$$

where $\tau_{eff} = \eta_{0,eff}/G_{0,eff}$ and the integration constant C depends on the flow protocol and initial condition.

SI.1.1 Particular solution for shear startup flow

Unlike in shear startup flows of the GCB model and in experiments of entangled WLMs, shear startup of two adjacent UCM fluids between parallel plates predicts shear-banded velocity profiles at all times in the flow if the rheological properties of fluids A and B are different. The particular solution to the shear stress equation SI.1.11 for a constant applied shear rate $\dot{\gamma}_0$ and solution initially at rest ($\sigma_{yx}(t=0) = 0$) is:

$$\sigma_{yx}(t) = \eta_{0,eff}\dot{\gamma}_0(1 - \exp(-t/\tau_{eff})) \tag{SI.1.12}$$

where $\dot{\gamma}_{app} = \dot{\gamma}_0$ is the applied shear rate in shear startup. The evolution of the shear stress has the same functional form as that of a single UCM fluid occupying the entire gap, except the zero-shear viscosity and relaxation time are replaced by effective values. However, unlike if only one UCM fluid occupied the gap, the shear rate is not constant and takes on different values in each fluid region A and B. The shear rates $\dot{\gamma}_A$ and $\dot{\gamma}_B$ are obtained by substituting the shear stress given by equation SI.1.12 into equations SI.1.5 and SI.1.6, respectively:

$$\dot{\gamma_A} = \dot{\gamma}_0 \left(\frac{\eta_{eff}}{\eta_A} - \left(\frac{\eta_{eff}}{\eta_A} + \frac{G_{eff}}{G_A} \right) \exp(-t/\tau_{eff}) \right) \tag{SI.1.13}$$

$$\dot{\gamma_B} = \dot{\gamma}_0 \left(\frac{\eta_{eff}}{\eta_B} - \left(\frac{\eta_{eff}}{\eta_B} + \frac{G_{eff}}{G_B} \right) \exp(-t/\tau_{eff}) \right) \tag{SI.1.14}$$

At $t = 0$, the shear rate of fluid i is equal to the ratio G_{eff}/G_i and at long times as $t \to \infty$ is equal to η_{eff}/η_i for the respective fluid $i = A, B$. The difference between the applied shear rate $\dot{\gamma}_0$ and the shear rate in either fluid region grows as the fluid properties become more dissimilar. This model predicts the shear rates in each region will be different almost immediately if the elastic moduli are different; however, in real shear-banding systems, some time is required for

heterogeneity to develop in the flow. Recall the adjacent UCM model is an approximation of steady shear-banded flow and therefore cannot make accurate predictions about the transient formation of flow heterogeneity and shear-bands.

SI.2 Germann-Cook-Beris model

For additional details, refer to [1,2].

$$\rho\frac{\partial \mathbf{v}}{\partial t} = -\rho\mathbf{v}\cdot\nabla\mathbf{v} - \nabla p + \nabla\cdot\boldsymbol{\sigma} \tag{SI.2.1}$$

$$\frac{\partial n_A}{\partial t} = -\nabla\cdot(\mathbf{v}\, n_A) - c_A\, n_A + \frac{1}{2}c_B n_B^2 \tag{SI.2.2}$$

$$\frac{\partial n_B}{\partial t} = -\nabla\cdot(\mathbf{v}\, n_B) + 2c_A\, n_A - c_B n_B^2 \tag{SI.2.3}$$

$$\frac{\partial \mathbf{C^A}}{\partial t} = -\nabla\cdot\left(\mathbf{v}\mathbf{C^A}\right) + \mathbf{C^A}\cdot\nabla\mathbf{v} - (\nabla\mathbf{v})^T\cdot\mathbf{C^A} - \frac{1}{\tau_A}\left(\mathbf{C^A} - \frac{n_A k_b\, T}{K_A}\mathbf{I}\right) - c_A\mathbf{C^A} + c_B n_B\mathbf{C^B} \tag{SI.2.4}$$

$$\frac{\partial \mathbf{C^B}}{\partial t} = -\nabla\cdot\left(\mathbf{v}\mathbf{C^i}\right) + \mathbf{C^i}\cdot\nabla\mathbf{v} - (\nabla\mathbf{v})^T\cdot\mathbf{C^i} - \frac{1}{\tau_B}\left(\mathbf{C^B} - \frac{n_B k_b\, T}{K_B}\mathbf{I}\right) + c_A\mathbf{C^A} - c_B n_B\mathbf{C^B} \tag{SI.2.5}$$

$$\boldsymbol{\sigma} = K_A\mathbf{C^A} - n_A k_B T\,\mathbf{I} + K_B\mathbf{C^B} - n_B k_B T\,\mathbf{I} + \eta_S\left(\nabla\mathbf{v} + (\nabla\mathbf{v})^T\right) \tag{SI.2.6}$$

$$c_A = c_{Aeq}\exp\left[\frac{\mathrm{Tr}\boldsymbol{\sigma^A}}{2n_A k_B T}\right] / \sqrt{\det\left(\mathbf{K_A}\mathbf{C^A}/n_A k_B T\right)} \tag{SI.2.7}$$

$$c_B = c_{Beq} \exp\left[\frac{\mathrm{Tr}\boldsymbol{\sigma}^{\boldsymbol{B}}}{n_B k_B T}\right] / \det\left(\mathbf{K_B}\mathbf{C^B}/n_B k_B T\right) \tag{SI.2.8}$$

Variables appearing in these equations are defined in Table S1. Equation SI.2.1 is the linear momentum balance. The evolution of the number densities of species A and B is given by equations SI.2.2 and SI.2.3. By mass conservation, the total number of species $n_A + \frac{1}{2}n_B$ is constant. Equations SI.2.4 and SI.2.5 describe the evolution of the conformation densities $\mathbf{C}^i = \mathbf{c}^i n_i$ of species $i = A, B$. In these equations, τ_A and τ_B are the relaxation times of species A and B, K_A and $K_B = 2K_A$ are the Hookean spring constants, k_b is Boltzmann's constant, and T is the absolute temperature.

Equation SI.2.6 describes the extra-stress tensor, where the first four terms are related to the extra stress of species A and B, and the last term is related to the viscous stress with solvent viscosity η_S. Equations SI.2.7 and SI.2.8 detail the breakage and reformation rates, where $c_{A,eq}$ and $c_{B,eq}$ are the equilibrium breakage and reformation rates at rest. In an equilibrium rest state ($\mathbf{v} = 0$, $p = 0$) with $c_A = c_{A,eq}$ and $c_B = c_{B,eq}$, the analytical solution to these equations is[3]: $n_A = n_A^0$, $n_B = n_B^0 = \sqrt{2n_A^0 c_{A,eq}/c_{b,eq}}$, $\mathbf{C}^i = (n_i^0 k_b T/K_i)\mathbf{I}$ for $i = A, B$.

SI.2.1 Non-dimensionalization

These equations are non-dimensionalized to produce the dimensionless variables and parameters in Table S2, which were used in prior work.[2].

The system of equations below assume 1D flow $v_r = v_z = 0$, negligible inertia $El^{-1} = 0$, the use of cylindrical coordinates (r, θ, z), and the non-dimensionalization in Table S2. **The '$\sim$' symbol over variables denoting dimensionless quantities is omitted for convenience.**

$$\frac{dn_A}{dt} = \frac{1}{\mu}\left(-c_A n_A + \frac{1}{2}c_b n_B^2\right) \tag{SI.2.9}$$

$$\frac{dn_B}{dt} = \frac{1}{\mu}\left(2c_A n_A - c_b n_B^2\right) \tag{SI.2.10}$$

Table S1: Key dimensional variables and parameters

Variable	Symbol
Fluid velocity	$\mathbf{v}$
Pressure	p
Extra-stress tensor	$\boldsymbol{\sigma}$
Number density of species i	n_i
Breakage rate	c_A
Reformation rate	c_B
Conformation density tensor	$\mathbf{C}^i$
Parameter	**Symbol**
Plateau modulus	G_0
Effective relaxation time	τ_{eff}
Density	ρ
Gap width	H
Inner cylinder tangential velocity	U_0
Hookean spring constant of species A	K_A
Equilibrium breakage rates	$c_{A,eq}$
	$c_{B,eq}$

where $i = A, B$

$$\frac{dC^A_{rr}}{dt} = \frac{1}{\mu}\left(-(C^A_{rr} - n_A) - c_A C^A_{rr} + c_B n_B C^B_{rr}\right) \tag{SI.2.11}$$

$$\frac{dC^A_{r\theta}}{dt} = C^A_{rr}\left(\frac{dv_\theta}{dr} - \frac{v_\theta}{r}\right) + \frac{1}{\mu}\left(-C^A_{r\theta} - c_A C^A_{r\theta} + c_B n_B C^B_{r\theta}\right) \tag{SI.2.12}$$

$$\frac{dC^A_{\theta\theta}}{dt} = 2C^A_{r\theta}\left(\frac{dv_\theta}{dr} - \frac{v_\theta}{r}\right) + \frac{1}{\mu}\left(-(C^A_{\theta\theta} - n_A) - c_A C^A_{\theta\theta} + c_B n_B C^B_{\theta\theta}\right) \tag{SI.2.13}$$

$$\frac{dC^A_{zz}}{dt} = \frac{1}{\mu}\left(-(C^A_{zz} - n_A) - c_A C^A_{zz} + c_B n_B C^B_{zz}\right) \tag{SI.2.14}$$

Table S2: Key dimensionless variables and parameters

Variable	Symbol	Expression
Time	$\tilde{t}$	$t/\tau_{eff} = t/\left[\tau_A/(1+c_{A,eq}\tau_A)\right]$
Spatial position	$\tilde{x}$	x/H
Radial coordinate	$\tilde{r}^*$	$r/H - 1/q$
Pressure	$\tilde{p}$	p/G_0 = p/$n_A^0 k_b T$
Number density	$\tilde{n}_i$	n_i/n_A^0
Reaction rates	$\tilde{c}_A$	$\tau_A c_A$
	$\tilde{c}_B$	$\tau_A c_B n_A^0$
Stress	$\tilde{\sigma}^i$	σ^i/G_0
Conformation density	$\tilde{\mathbf{C}}^i$	$\mathbf{C}^i(K_A/G_0)$
Parameter	**Symbol**	**Expression**
Elasticity number	El	$G_0\tau_{eff}^2/\rho H^2$
Viscosity ratio	β	η_S/η_0
Relaxation time ratios	ϵ	τ_B/τ_A
	μ	τ_A/τ_{eff}
Equilibrium reaction rates	$\tilde{c}_{Aeq}$	$\tau_A c_{Aeq}$
	$\tilde{c}_{Beq}$	$\tau_A c_{Beq} n_A^0$
Curvature	q	$(R_o - R_i)/R_i$
Weissenberg number	Wi	$\tau_{eff} U_0/H$

$$\frac{dC_{rr}^B}{dt} = \frac{1}{\epsilon\mu}\left(-(C_{rr}^B - \frac{1}{2}n_B) + \epsilon(c_A C_{rr}^A - c_B n_B C_{rr}^B)\right) \tag{SI.2.15}$$

$$\frac{dC_{r\theta}^B}{dt} = C_{rr}^B\left(\frac{dv_\theta}{dr} - \frac{v_\theta}{r}\right) + \frac{1}{\epsilon\mu}\left(-C_{r\theta}^B + \epsilon(c_A C_{r\theta}^A - c_B n_B C_{r\theta}^B)\right) \tag{SI.2.16}$$

$$\frac{dC_{\theta\theta}^B}{dt} = 2C_{r\theta}^B\left(\frac{dv_\theta}{dr} - \frac{v_\theta}{r}\right) + \frac{1}{\epsilon\mu}\left(-(C_{\theta\theta}^B - \frac{1}{2}n_B) + \epsilon(c_A C_{\theta\theta}^A - c_B n_B C_{\theta\theta}^B)\right) \tag{SI.2.17}$$

$$\frac{dC^B_{zz}}{dt} = \frac{1}{\epsilon\mu}\left(-(C^B_{zz} - \frac{1}{2}n_B) + \epsilon(c_A C^A_{zz} - c_B n_B C^B_{zz})\right) \tag{SI.2.18}$$

These time evolution equations govern the number densities of species A and B along with the conformation tensors. The velocity is specified by the momentum balance:

$$0 = \frac{dC^A_{r\theta}}{dr} + 2\frac{dC^B_{r\theta}}{dr} + \beta\left[\frac{d^2 v_\theta}{dr^2} - \frac{dv_\theta}{dr}\frac{1}{r} + \frac{v_\theta}{r^2}\right] + 2\frac{\sigma_{r\theta}}{r} \tag{SI.2.19}$$

In the above equations, the remaining unknown quantities are provided by the following relations. Shear stress is given by:

$$\sigma_{r\theta} = C^A_{r\theta} + 2C^B_{r\theta} + \beta\left(\frac{dv_\theta}{dr} - \frac{v_\theta}{r}\right) \tag{SI.2.20}$$

and the reaction rates are:

$$c_A = c_{Aeq}\exp\left[\frac{\mathrm{Tr}\boldsymbol{\sigma}^{\boldsymbol{A}}}{2n_A}\right]/\sqrt{\det\left(\mathbf{C}^{\mathbf{A}}/n_A\right)} \tag{SI.2.21}$$

$$c_B = c_{Beq}\exp\left[\frac{\mathrm{Tr}\boldsymbol{\sigma}^{\boldsymbol{B}}}{n_B}\right]/\det\left(2\mathbf{C}^{\mathbf{B}}/n_B\right) \tag{SI.2.22}$$

where $\boldsymbol{\sigma}^{\boldsymbol{A}} = \mathbf{C}_A - n_A\mathbf{I}$ and $\boldsymbol{\sigma}^{\boldsymbol{B}} = 2\mathbf{C}_B - n_B\mathbf{I}$

The boundary condition in dimensionless form is:

$$\tilde{v_\theta}(\tilde{r}^* = 0) = Wi_{app}\tanh(at) \tag{SI.2.23}$$

SI.2.2 Numerical solution

The r-domain was discretized using a Chebyshev pseudospectral collocation method.[4,5] A total of $N = 200$ collocation points was used for discretization similar to prior work[2]. The resulting set of ordinary differential equations was integrated in time using the MATLAB ode15s variable-step, variable-order solver.[6]

SI.3 Additional rheology details

The rheological properties of P234-NaCl and P234-NaF are very different, thus distinct rheology protocols were used. P234-NaCl rheology is very sensitive to the thermal treatment and sample age[7]; thus the pre-shear, thermal treatment, and rejuvenation protocols are almost identical to those in Ref. 7. In brief, the sample was rejuvenated between measurements by switching to a chiller operating at 20 °C. The sample was sheared continuously $\dot{\gamma} = 1$ s^{-1} at 20 °C for five minutes followed by a five-minute rest period to destroy any residual structure. Then the flow cell was reattached to the heat bath (38.5 $\pm$ 0.1 °C) to heat the sample and reform WLMs.

The formation and growth of P234-NaCl WLMs at 38.5 °C were monitored by continuous small amplitude oscillatory shear (SAOS) at strain amplitude and frequency $\gamma_0 = 1$ % and $\omega = 1$ rad/s, respectively. Prior to nonlinear rheology, the sample was aged until the storage modulus reached $G' = 24$ Pa, the same value as in Ref. 7 when D_2O was used as a solvent. Evaporation had a minimal effect between trials, as frequency sweeps ($\gamma_0 = 1$ %, $\omega = 1 - 10$ rad/s) before each trial were nearly identical. Flow curves were measured using both controlled stress (creep) and controlled shear rate protocols. Creep measurements were performed for 2 - 3 h at shear stresses $\sigma = 1 - 15$ Pa. The low-shear rate region ($\dot{\gamma} = 0.02 - 0.0005$ s^{-1}) was measured via a ramp-down protocol where the shear rate was incrementally reduced, measuring the stress response for 2 h before proceeding to the next shear rate. Shear startup tests, where the shear rate is increased suddenly to a constant value from rest, captured the flow curve behavior at higher $\dot{\gamma} = 0.1$ and 0.5.

For P234-NaF, a ten-minute equilibration period at $T = 43.5$ °C preceded all measurements, also monitored with SAOS ($\gamma_0 = 1$%, $\omega = 1$ rad/s). The sample was rejuvenated between trials using the same cooling protocol applied to P234-NaCl. The P234-NaF flow curve was measured to identify the likely shear banding region. These WLMs did not have a yield stress, thus a single ramp-up shear rate protocol ($\dot{\gamma} = 0.02 - 10$ s^{-1}) captured both the Newtonian region (low $\dot{\gamma}$) and the shear-banding plateau (intermediate $\dot{\gamma}$). The onset of the shear banding plateau agreed with the expected value for viscoelastic WLMs $\dot{\gamma}\tau \sim 1$[8], where the relaxation time τ was calculated from the crossover of G' and G'', measured in a frequency sweep.

SI.4 Velocity estimation from particle trajectory fits

The desired information from rheo-PTV measurements is the velocities of a set of particles at time points of interest, which can be sorted by gap position to construct velocity profiles. However, the measured data from rheo-PTV experiments are the particle positions, $\mathbf{x}^i = (x^i(t), y^i(t))$ for each particle i. Therefore, the goal of rheo-PTV analysis is to estimate for each particle the velocity, $\mathbf{v}^i(t)$, which satisfies the kinematics equation:

$$\mathbf{x}^i(t) = \mathbf{x}_0^i + \int_{t=0}^{t} \mathbf{v}^i(t)dt \tag{SI.4.1}$$

where $\mathbf{x}_0^i$ is the initial position and $\mathbf{v}^i(t)$ the velocity vector. This work assumes two functional forms for $\mathbf{v}^i(t)$. For calculations over short time intervals – such that a particle's velocity does not change significantly – the velocity is assumed to be roughly constant and equal to an average value: $\mathbf{v}^i(t) \approx \mathbf{v}_{avg}^i$. The expected value of the particle position at time t_n is then:

$$E(t_n) = \mathbf{x}_0^i + \mathbf{v}_{avg}^i(t_n - t_0) \tag{SI.4.2}$$

The value of $\mathbf{v}_{avg}^i(\mathbf{x}^i)$ is estimated by minimizing the sum of the residuals of the known and predicted positions along the particle trajectory from $t = t_0$ to t_{N-1}: $\mathbf{T}^i = (\mathbf{x}_0^i, \mathbf{x}_1^i, ..., \mathbf{x}_{N-1}^i)$ with N recorded positions within the time interval. The following sum is minimized, which is analogous to fitting the particle trajectory by varying $\mathbf{v}_{avg}^i(\mathbf{x}^i)$ and x_0^i:

$$\sum_{n=1}^{N-1} \mathbf{x}^i(t_n) - E(t_n) = \sum_{n=1}^{N-1} (\mathbf{x}^i(t_n) - \mathbf{x}_0^i) - \mathbf{v}_{avg}^i(t_n - t_0) \tag{SI.4.3}$$

The flows in this study follow arced trajectories that are concentric with the inner and outer cylinders, and therefore representing particle positions in polar coordinates (r, θ) is more convenient. In this coordinate system, the particle velocities are nearly one-dimensional such that the average velocity along the radial coordinate can be assumed to be zero: $\mathbf{v}_{avg,r}^i = 0$. The residual equation SI.4.4 can be rewritten as:

$$\sum_{n=1}^{N-1} s^i(t_n) - E(t_n) = \sum_{n=1}^{N-1} (s^i(t_n) - s_0^i) - v_{avg,\theta}^i (t_n - t_0) \tag{SI.4.4}$$

where $s(t_n) = r\theta(t_n)$ is the arc-length relative to the positive x-axis.

For cessation of flow experiments where particles continuously decelerate, functions of exponentials were also used to model particle displacement, d, relative to the position at t_0. The specific functions are detailed in sections SI.4.2 and SI.4.3. The velocity is calculated from these displacement functions:

$$d(t) = s^i(t) - s_0^i = \int_{t=0}^{t} v_\theta^i(t) dt \tag{SI.4.5}$$

$$\frac{d}{dt} d(t) = v_\theta^i(t) \tag{SI.4.6}$$

SI.4.1 Comparison of trajectory fitting vs. standard PTV analysis

The key advantage of the trajectory fitting approach is that it produces a more representative estimate of the uncertainty of the particle velocity compared to standard PTV analysis. In the standard PTV analysis method, the average velocity of a particle over a time interval is estimated from displacements between successive image acquisitions:

$$v_{\theta,avg} = \frac{1}{N-1} \sum_{n=1}^{N-1} \frac{(s^i(t_n) - s^i(t_{n-1}))}{\Delta t} = \frac{1}{N-1} \sum_{n=1}^{N-1} v_{\theta,n}^i \tag{SI.4.7}$$

where $s^i(t_n) - s^i(t_{n-1})$ is the displacement of a particle between two images recorded at times t_n and t_{n-1}, and $\Delta t = t_n - t_{n-1}$ is the time elapsed between image acquisitions (the inverse of the framerate). Over the same time interval, both approaches provide similar estimates of a particle velocity (Figure S1), but the uncertainties of the velocities calculated from the standard PTV analysis, which is the standard deviation of the particle velocities from $v_{\theta,avg}$, are significantly larger. With these uncertainty values, differentiating reliable data from experimental noise is challenging. Unpacking the reason for this difference is beyond the scope of this work and is discussed in detail

elsewhere[9]. Briefly, careful analysis of the uncertainty reveals that the standard deviation used in the standard PTV analysis is not the appropriate metric for the velocity uncertainty.

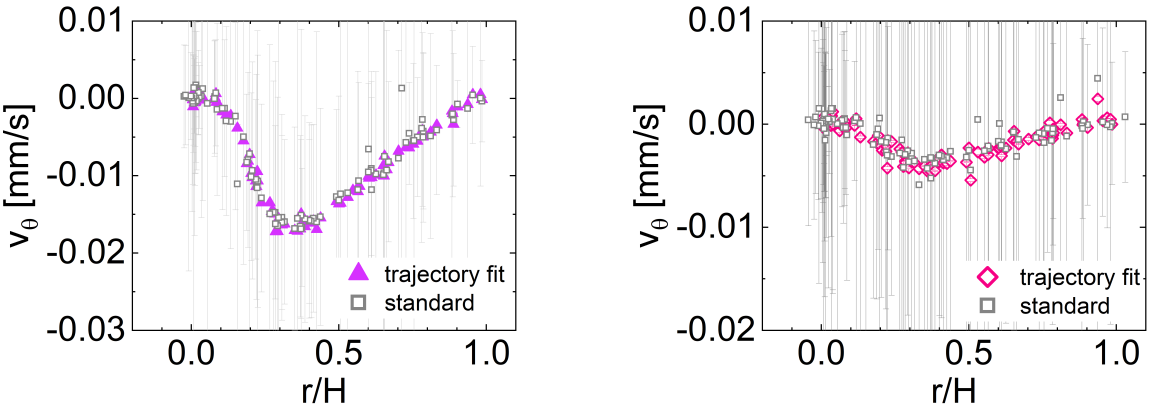

Figure S1: Comparison of velocity profiles ((c) and (d) in Figure S12) calculated using the trajectory fitting approach, assuming an average velocity over a short time interval, and the standard PTV analysis of calculating velocities from displacements between successive image acquisitions and averaging these over a short time interval.

SI.4.2 Cessation of flow displacement fits: P234-NaF

Particle trajectories for P234-NaF were fit with two functions. For $t_c = 3$ and 540 seconds, a single exponential function was fit to the trajectories:

$$d = A \exp\left(\frac{-t}{\tau_v}\right) + D \tag{SI.4.8}$$

where d is the displacement of the particle, τ_v is the relaxation time, and A and D are constants that depend on the magnitude of the displacement. A sample fit of this model to a particle trajectory is shown in Figure S2a. Given this equation for the displacement, the equation for the particle velocity is:

$$v_\theta = -\frac{A}{\tau_v} \exp\left(\frac{-t}{\tau_v}\right) \tag{SI.4.9}$$

For the cessation of flow trial that begins at $t_c = 14$ s, the displacement could not be described

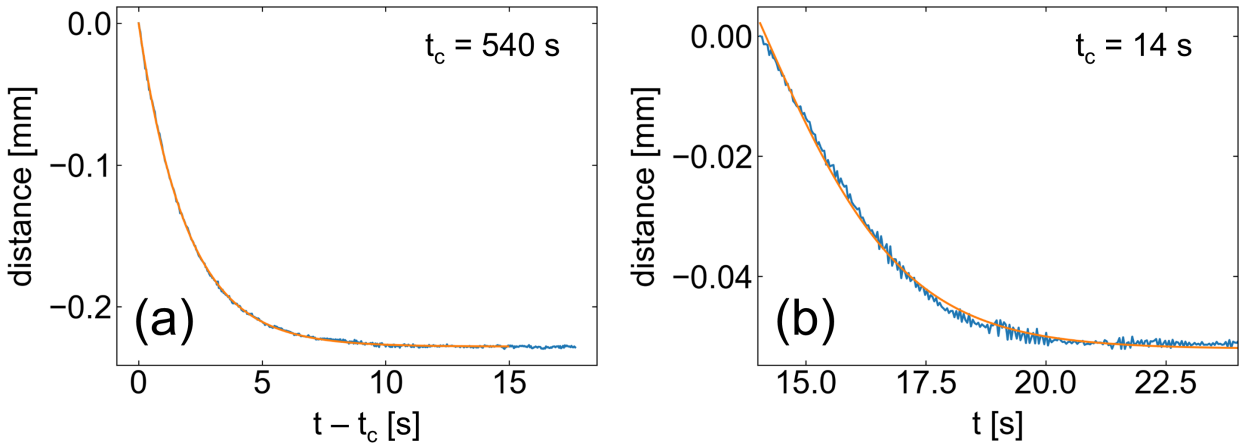

Figure S2: Sample particle trajectories fit with a single relaxation time exponential decay (a) and a sigmoid decay (b). Particle trajectories for $t_c = 3$ and 540 s were fit with an exponential decay function and for $t_c = 14$ with a sigmoid function.

by an exponential function. Instead, a sigmoid function was fit to these trajectory data:

$$d = \frac{A}{1 + \exp(t/\tau_v)} + D \tag{SI.4.10}$$

The corresponding equation for the velocity is:

$$v_\theta = \frac{-A \exp(t/\tau_v)}{\tau_v \left[1 + \exp(t/\tau_v)\right]^2} \tag{SI.4.11}$$

After a few relaxation times, equation SI.4.11 converges toward the velocity equation SI.4.9:

$$v_\theta = \frac{-A \exp(t/\tau_v)}{\tau_v \left[1 + \exp(t/\tau_v)\right]^2} \approx v_\theta = -\frac{A}{\tau} \exp\left(\frac{-t}{\tau_v}\right) \tag{SI.4.12}$$

An example fit of the sigmoid function to a particle trajectory for $t_c = 14$ s is shown in Figure S2b. The particle trajectory may relax differently in this case due to the substantial positive motion of the thin fluid layers at either cylinder boundary, which competes with the retraction in the bulk (Figure S11a).

An ensemble of trajectories spanning the gap was fit with these displacement functions. For these P234-NaF trials, the motion of 0.1 mm boundary layers near either cylinder wall was not fitted. The time constants from each trajectory were averaged and are shown in Table 2 in the main

text. Greater than sixty time constants were averaged in each case.

SI.4.3 Cessation of flow displacement fits: P234-NaCl

Particle trajectories for all P234-NaCl trials were fit with a sum of two exponentials:

$$d = A\exp(-t/\tau_{v,1}) + C\exp(-t/\tau_{v,2}) + D \tag{SI.4.13}$$

where similar to the P234-NaF fits, d is the particle displacement, $\tau_{v,1}$ and $\tau_{v,2}$ are time constants, A, C, and D are constants related to the magnitude of the displacement. The corresponding velocity of the particle is given by:

$$v_\theta = -\frac{A}{\tau_{v,1}}\exp\left(\frac{-t}{\tau_{v,1}}\right) - \frac{C}{\tau_{v,2}}\exp\left(\frac{-t}{\tau_{v,2}}\right) \tag{SI.4.14}$$

An example fit of the particle trajectory for P234-NaCl is shown in Figure S3. The two exponential model fits the displacement data reasonably well, except for a brief period of rapid retraction at the onset of cessation of flow. Similar to the P234-NaF trials, an ensemble of trajectories was fit to compute average time constants.

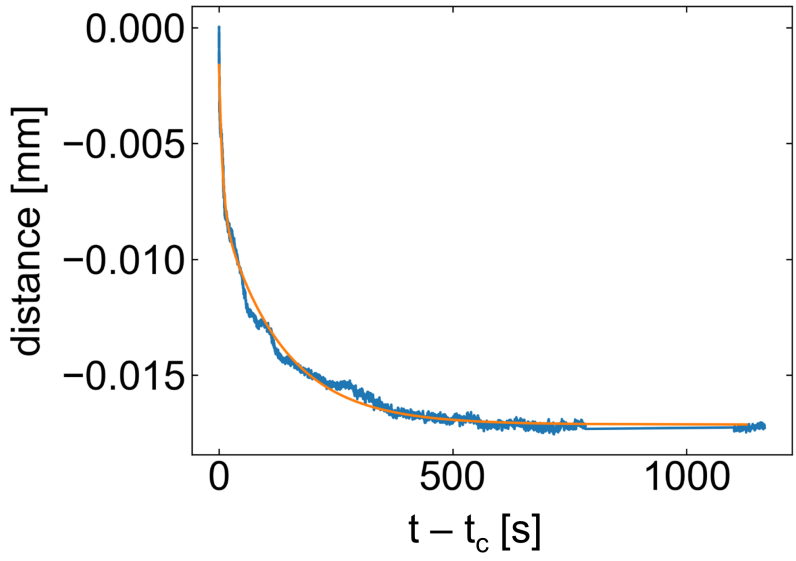

Figure S3: Sample particle trajectory fit with a sum of two exponentials with time constants $\tau_{v,1}$ and $\tau_{v,2}$.

SI.4.4 Comparison of velocity profiles obtained by fitting full-trajectories vs. trajectory segments

Comparison of velocity profiles calculated during cessation of flow by fitting full-duration trajectories with an exponential-type function or by fitting a segment of the trajectory over a short time interval assuming a constant velocity, which is the approach used in shear startup. The velocity profiles obtained with both approaches agree favorably (Figure S4). Fitting an exponential-type function across a broad time range is advantageous because the velocity can easily be calculated at any time from the fits. However, this approach could not be applied to all particles. In particular, particles near the boundaries in P234-NaF could not be well-described by decaying exponentials. Additionally, this approach neglects particles tracked for shorter durations. In these cases, particle velocities in cessation of flow must be calculated over short time intervals assuming a roughly constant velocity. The length of the averaging interval was informed by the fits of entire particle trajectories; as the particles slowed down, the averaging time increased.

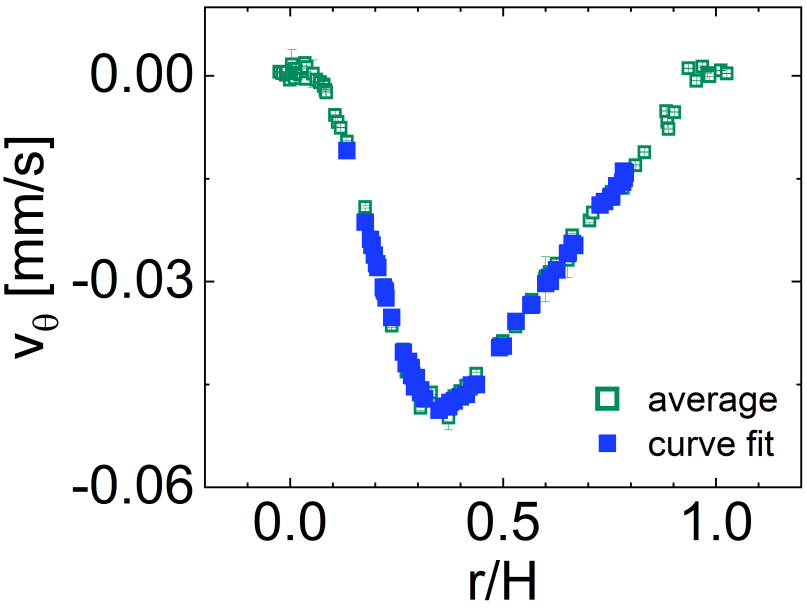

Figure S4: Sample velocity profiles in cessation of flow obtained using two methods. In one method, particle trajectories were fit over short intervals in which an average particle velocity was assumed. The other method fits entire particle trajectories assuming a decaying exponential functional form (see Section SI.4), and the velocity is computed at a certain time from this function. The results of both approaches agree favorably.

SI.4.5 Variation of particle relaxation time with gap position

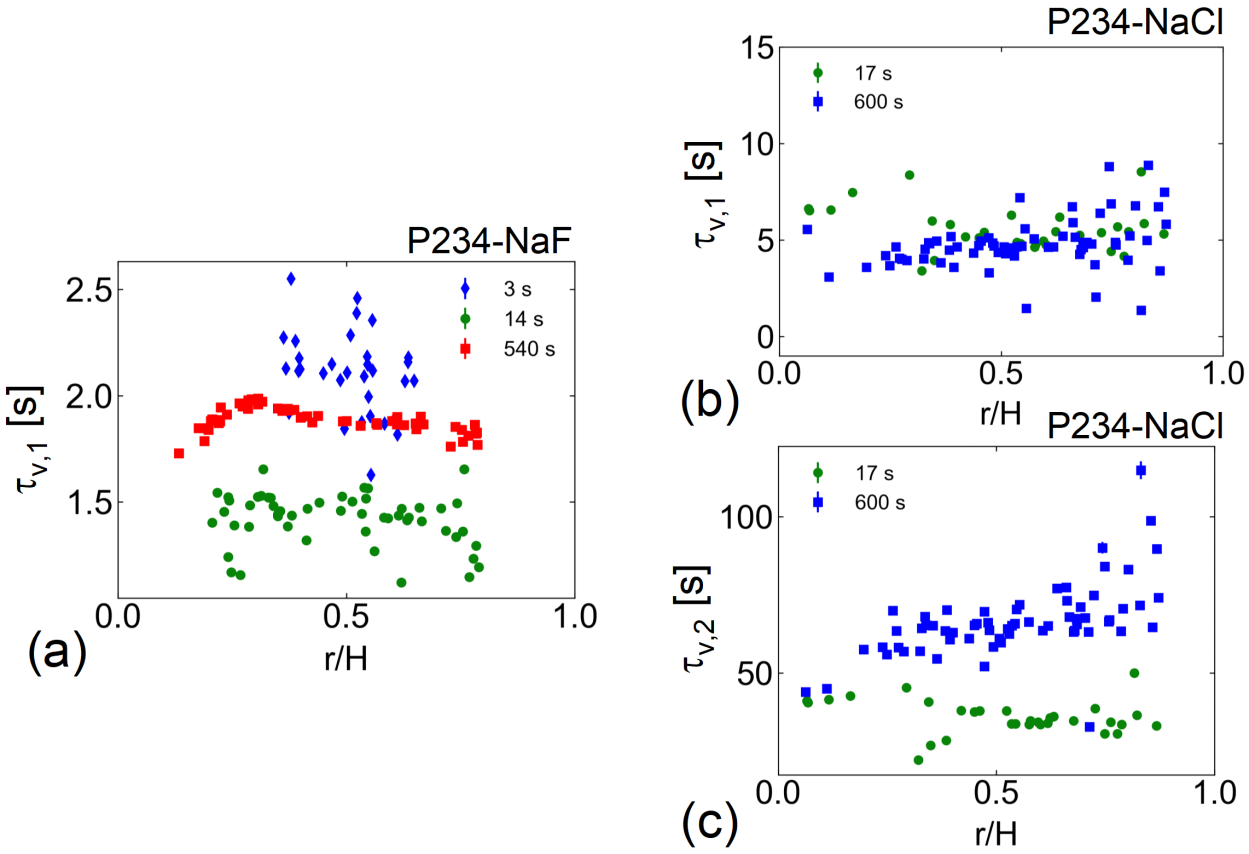

Figure S5: (a) Relaxation of the particle velocity, $\tau_{v,1}$, as a function of gap position, r/H, for P234-NaF at $t_c = 3$, 14, and 540 s. (b) and (c) Relaxation times $\tau_{v,1}$ and $\tau_{v,2}$ as a function of gap position for P234-NaCl at select $t_c = 17$ and 600 s. Across both samples and all t_c (including trials not shown), the relaxation time tends to have the least scatter near the center of the geometry or the interface between heterogeneous regions where the particle velocities are greatest. The relaxation times of particles near the boundaries could not be estimated due to the low signal-to-noise ratio as particles near the wall are nearly immobile. Furthermore, the velocities of particles near the inner cylinder are difficult to determine for higher t_c due to strong WLM alignment near the inner boundary, leading to substantial scattering of the light reflected from the particles.[7]

SI.5 Shear startups and velocity profiles before cessation of flow

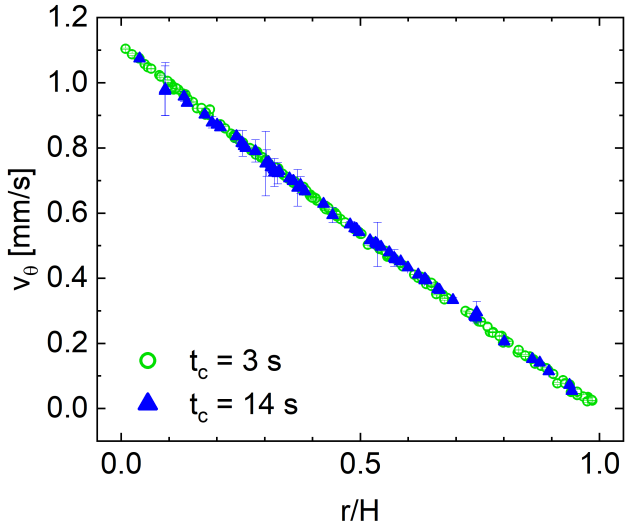

Figure S6: Velocity profile immediately before cessation of flow of P234-NaF for t_c =3 and 14 seconds. The velocity profile is nearly linear in both cases, consistent with the full-length startup in Figure 3c.

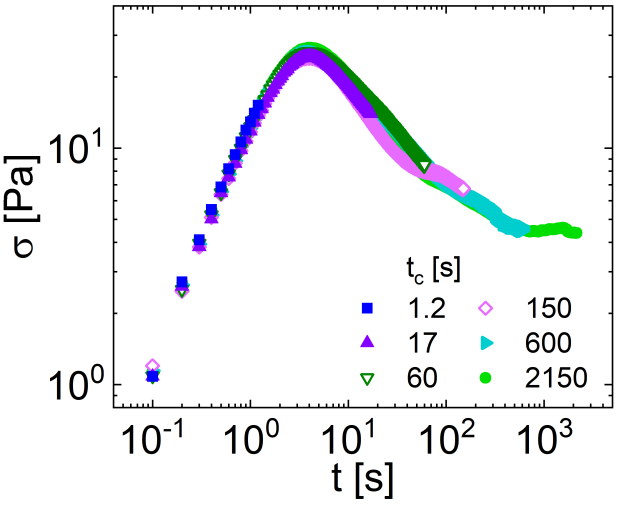

Figure S7: Shear startups of P234-NaCl performed prior to cessation of flow ending at t_c =1.2, 17, 60, 150, 600, and 2150 seconds. The shear startups ending at t_c = 1.2, 17, and 2150 seconds are also plotted in the main text Figure 5a. The evolution of the shear stress agrees across trials.

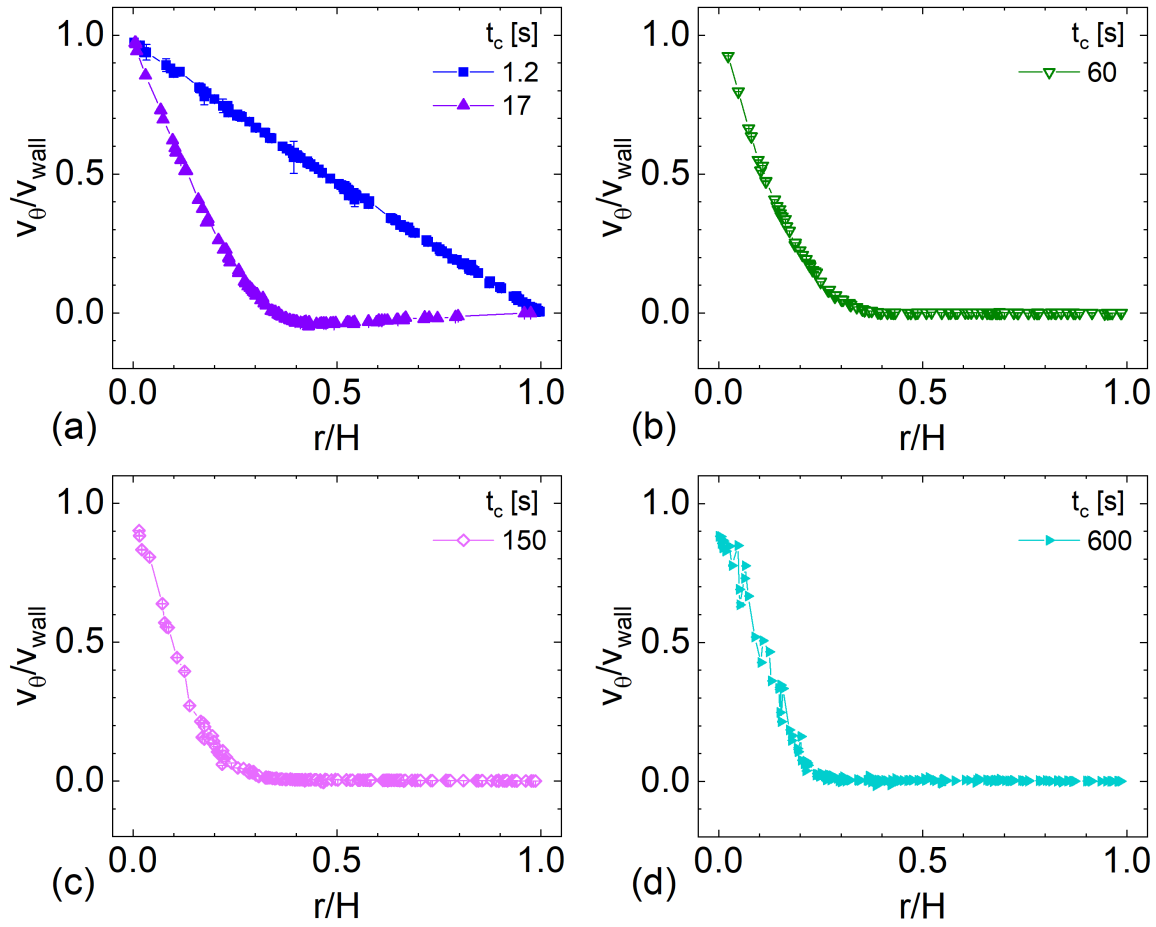

Figure S8: Velocity profiles immediately before cessation of flow of P234-NaCl for (a) t_c =1.2 and 17, (b) $t_c = 60$, (c) $t_c = 150$, and (d) $t_c = 600$ seconds. These velocity profiles in these shorter-length startups are consistent with the full-length startup ($t_c = 2150$ s) in Figure 3.

SI.6 Comparison of 15% wt P234 with 2M NaCl in water vs. D_2O

The rheology of 15% wt P234 with 2M NaCl was analyzed in depth with D_2O as a solvent in prior work.[7] Here, water is used as a solvent and the supplier of the poloxamer is different. Whereas the stress plateaued with decreasing applied shear rate in this previous work,[7] here a distinct region of changing shear stress at low shear rates is observed. The shear stress appears to plateau briefly with decreasing applied shear rate, and the value of the shear stress in this small plateau region is similar in value to the dynamic yield stress reported previously.[7] Here, the variation in shear stress at the lowest shear rates could actually represent a new regime of behavior or could be an artifact from insufficient measurement time or sample evaporation. Further consideration of this region is deferred to future study. However, for comparison to prior work, a frequency sweep of P234-NaCl in water at 38.5 °C is shown below in Fig. S9, following aging until the storage modulus reached $G' = 24$ Pa (same value as in Ref. 7 when D_2O was used as a solvent).

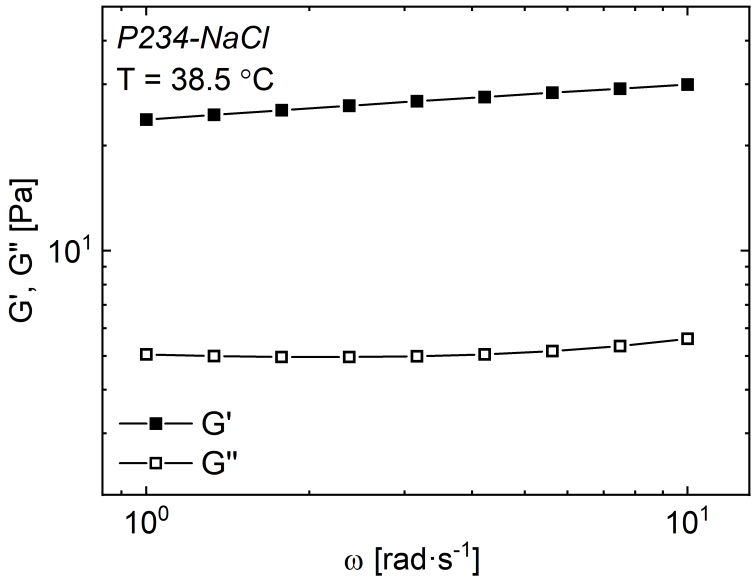

Figure S9: Frequency sweep of P234-NaCl at 38.5 °C following aging

SI.7 Individual cessation of flow velocity profiles

Velocity profiles for individual cessation of flow trials for P234-NaF and P234-NaCl are shown below. For trials in which the flow was stopped after heterogeneous flow had already formed, interesting behaviors with respect to the gap position, r/H, of the maximum retraction magnitude are observed.

For example, for stop times near the onset of heterogeneous flow like in P234-NaCl at 17 s (Fig. S13) and P234-NaF at 540 s (Fig. S12), a slight shift to lower r/H in time as the retraction magnitude decreases; this trend is consistent with GCB model predictions when the flow is also stopped at early times before the band interface is sharp (Fig. 9e). The movement of the interface position to slightly lower r/H as the band interface becomes sharper is also observed upon shear startup in the GCB model (Fig. 8).

However, when the heterogeneous flow regions are fully formed and a sharp interface has formed between regions prior to stopping flow, no change in interface position is observed in GCB simulations upon flow cessation (Figs. 9f, S23). In experiments, a shift in the maximum retraction magnitude occurs toward higher (not lower) r/H (Figs. S14 -S17). This shift to higher r/H after longer stop times is not captured by the GCB model.

SI.7.1 P234-NaF

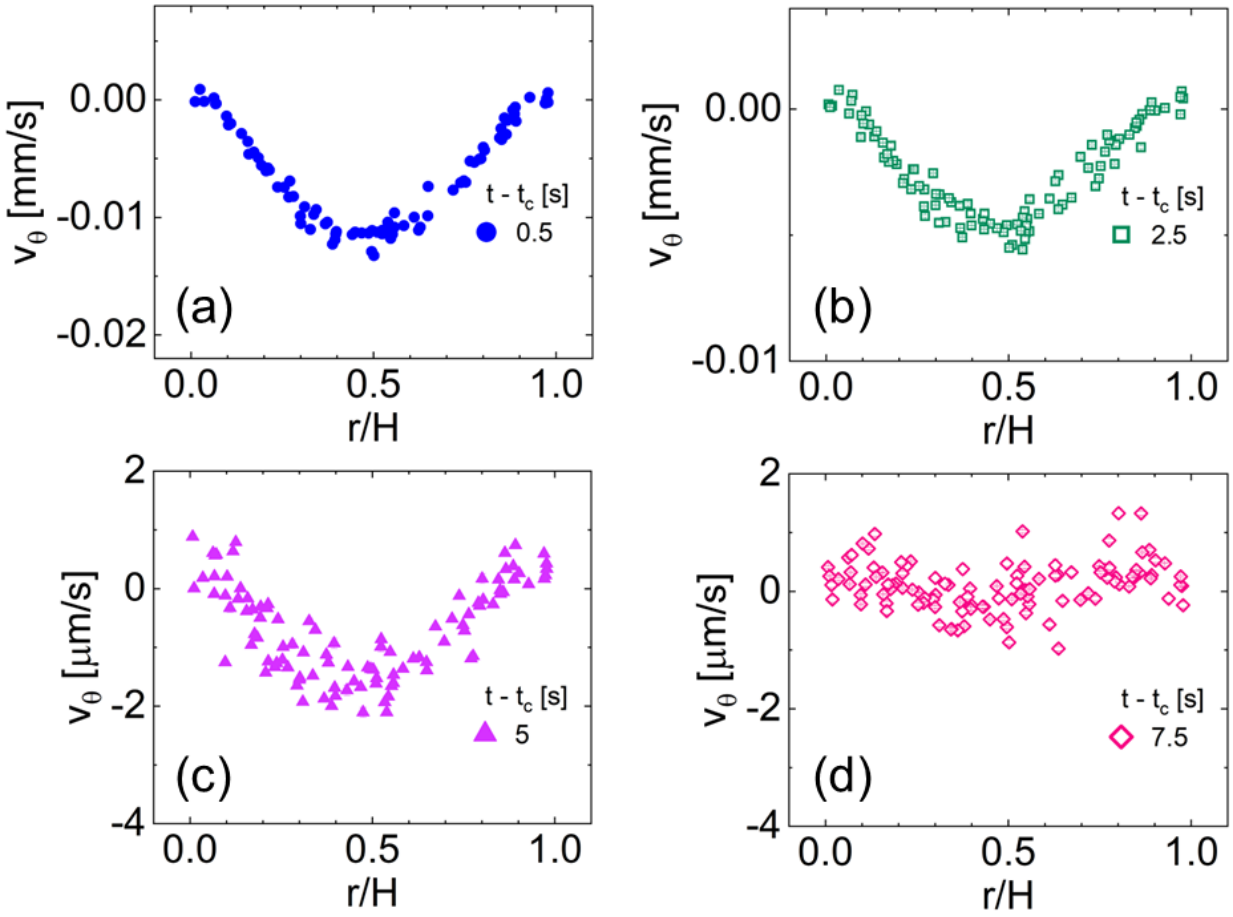

Figure S10: Velocity profiles of P234-NaF after $t_c = 3$ s of shear startup flow at $\dot{\gamma} = 1$ s^{-1}. These velocity profiles are plotted together in Figure 4e in the main text. Note the y-axis scale may differ between panels.

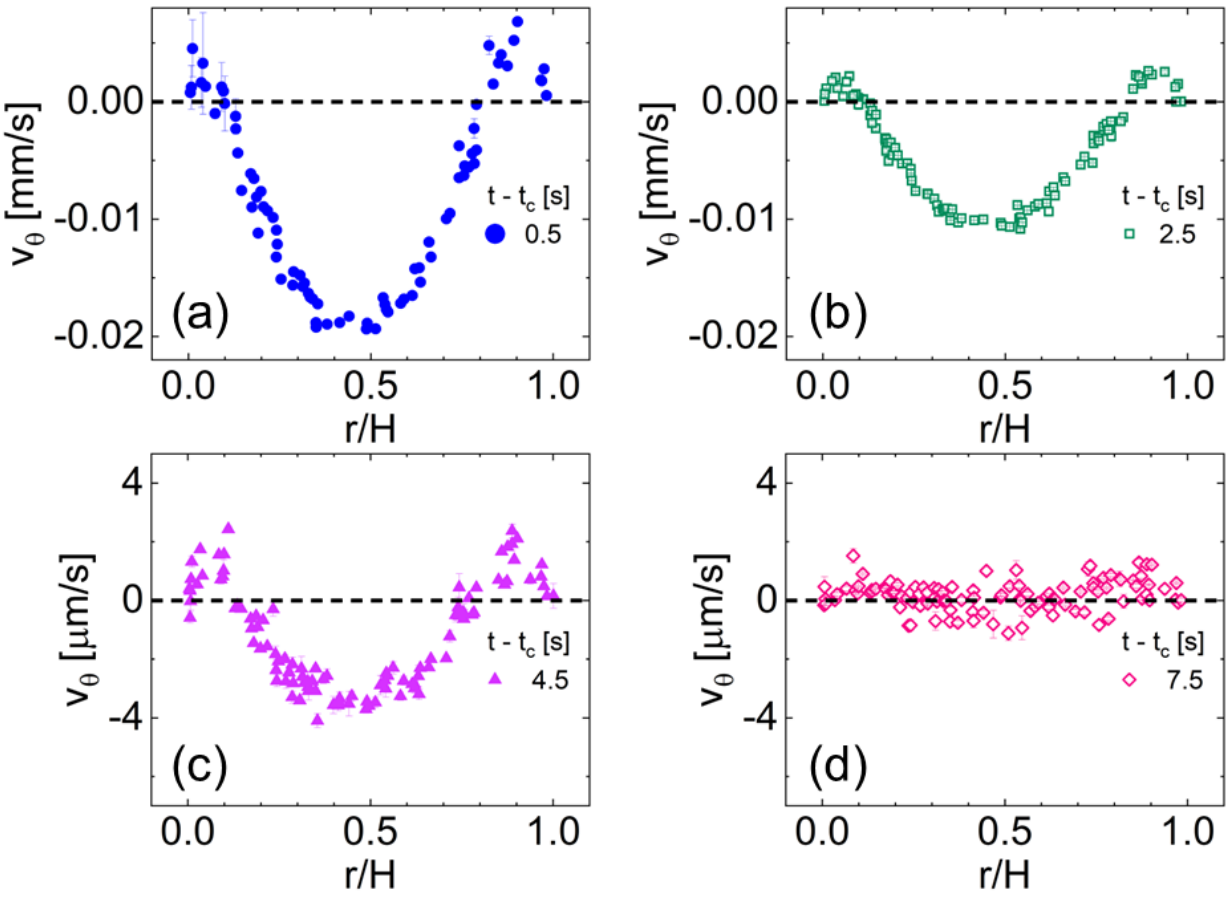

Figure S11: Velocity profiles of P234-NaF after $t_c = 14$ s of shear startup flow at $\dot{\gamma} = 1$ s^{-1}. These velocity profiles are plotted together in Figure 4f in the main text. Note the y-axis scale may differ between panels.

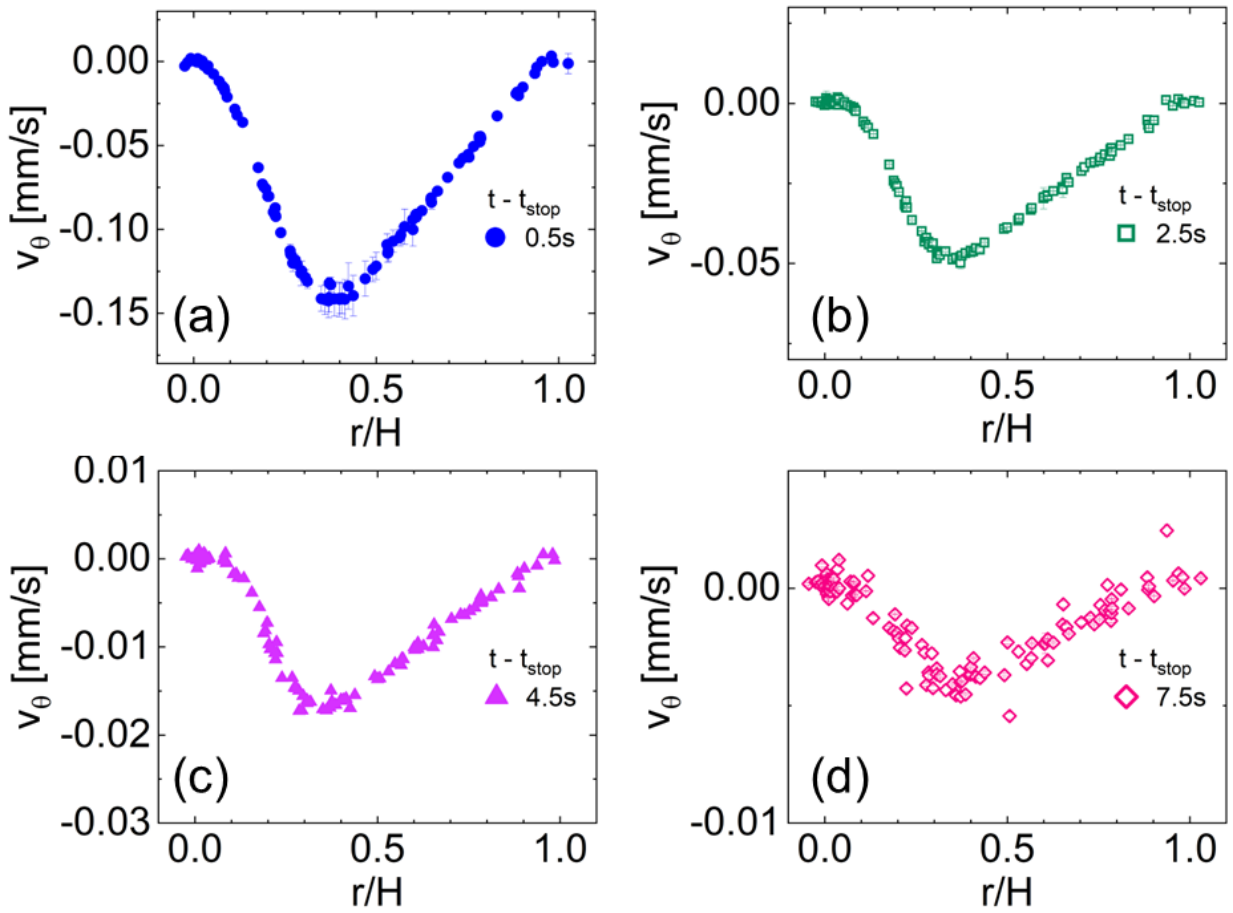

Figure S12: Velocity profiles of P234-NaF after $t_c = 540$ s of shear startup flow at $\dot{\gamma} = 1$ s^{-1}. These velocity profiles are plotted together in Figure 4g in the main text. Note the y-axis scale may differ between panels.

SI.7.2 P234-NaCl

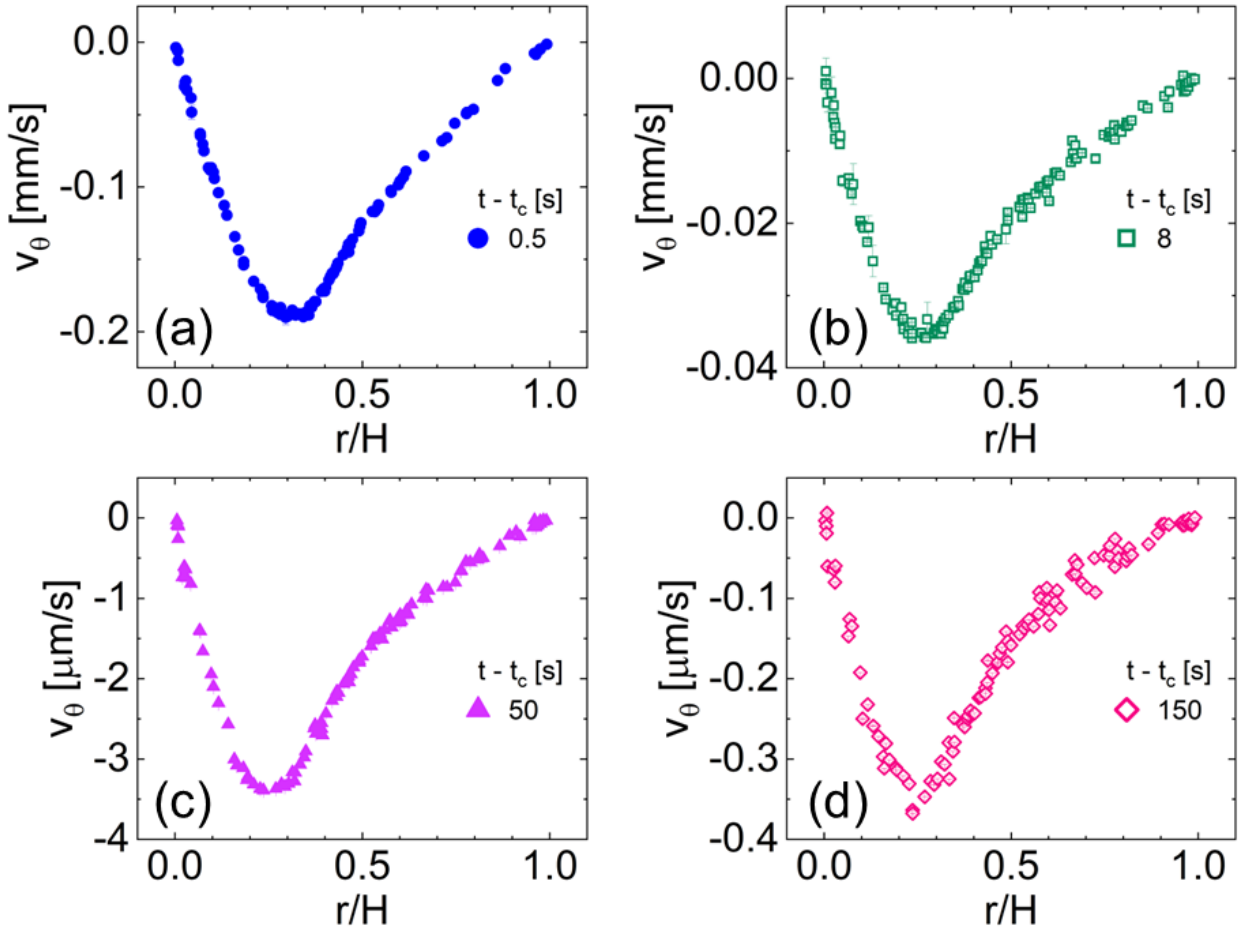

Figure S13: Velocity profiles of P234-NaCl after $t_c = 17$ s of shear startup flow at $\dot{\gamma} = 0.5$ s^{-1}. These velocity profiles are plotted together in Figure 5f in the main text. Note the y-axis scale may differ between panels.

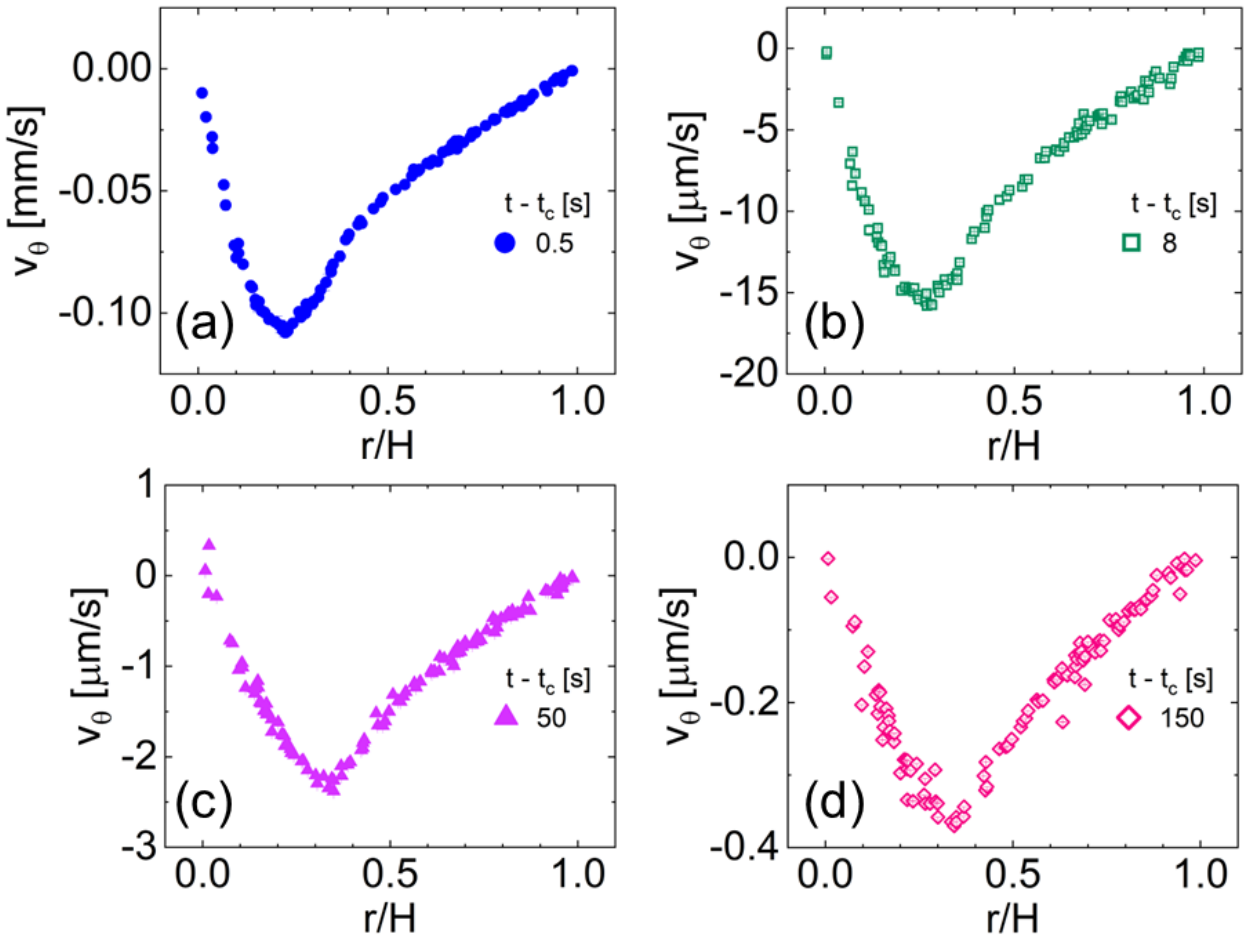

Figure S14: Velocity profiles of P234-NaCl after $t_c = 60$ s of shear startup flow at $\dot{\gamma} = 0.5$ s^{-1}. These velocity profiles are plotted together in Figure S22d in Section SI.9. Note the y-axis scale may differ between panels.

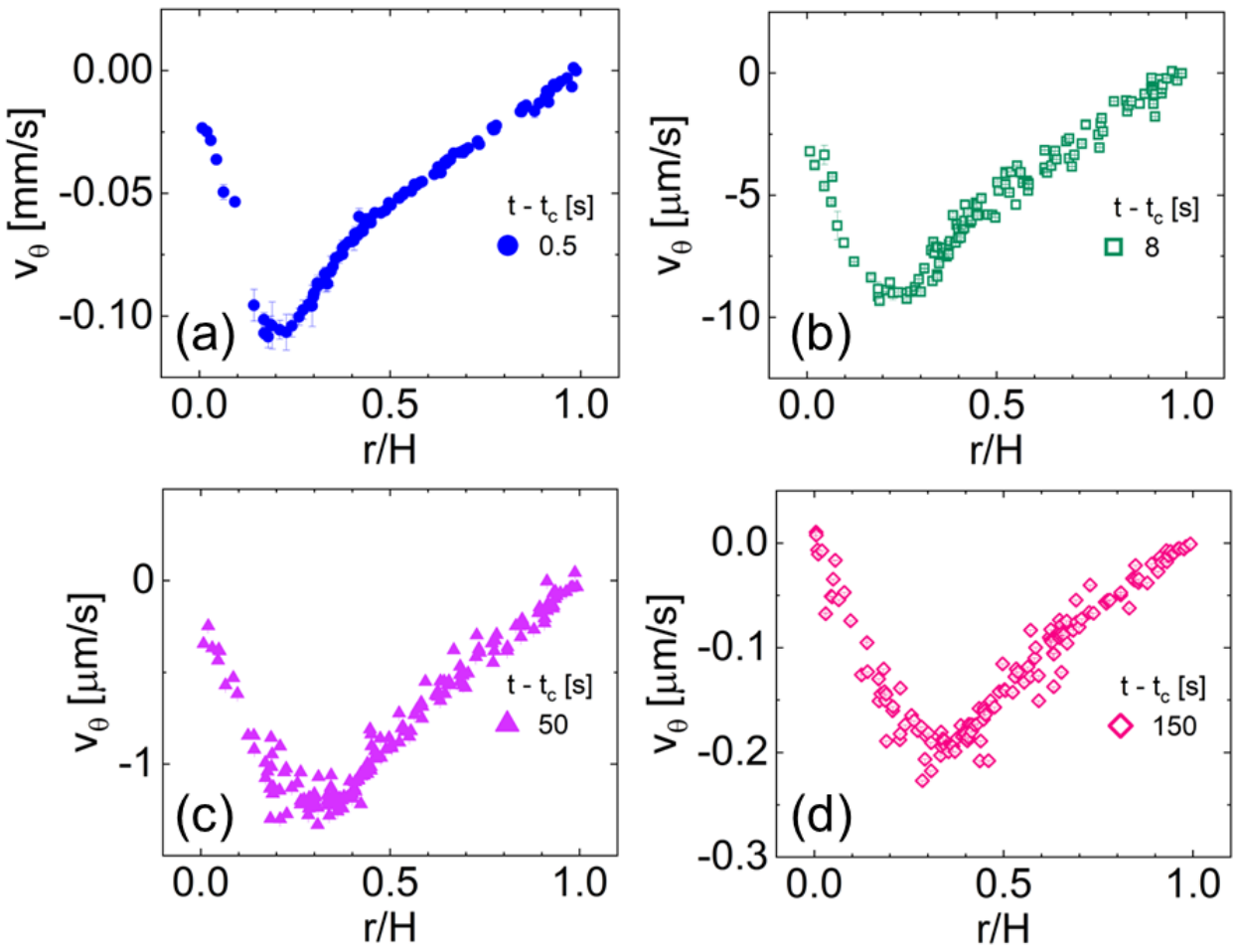

Figure S15: Velocity profiles of P234-NaCl after $t_c = 150$ s of shear startup flow at $\dot{\gamma} = 0.5$ s^{-1}. These velocity profiles are plotted together in Figure S22e in Section SI.9. Note the y-axis scale may differ between panels.

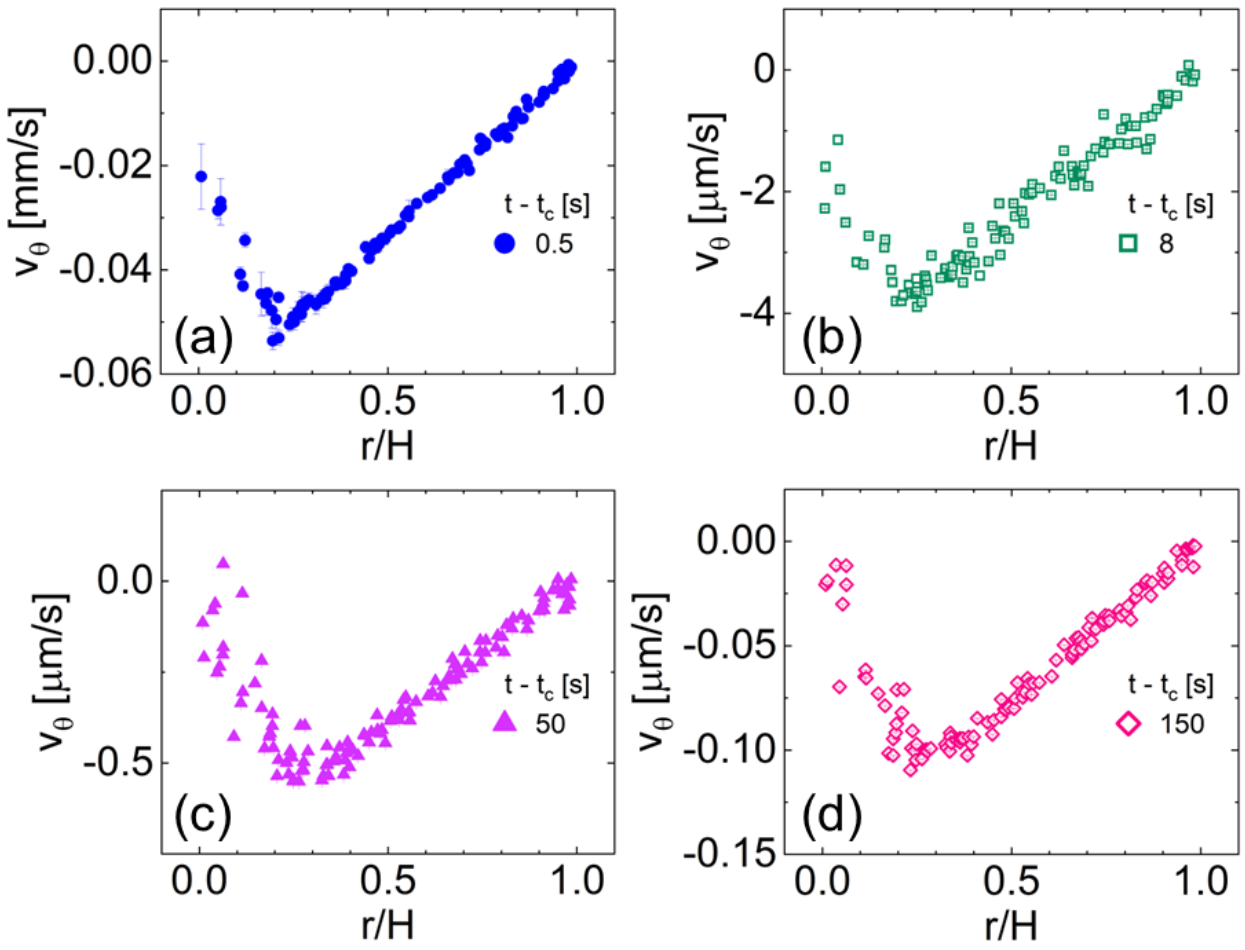

Figure S16: Velocity profiles of P234-NaCl after $t_c = 600$ s of shear startup flow at $\dot{\gamma} = 0.5$ s^{-1}. These velocity profiles are plotted together in Figure S22f in Section SI.9. Note the y-axis scale may differ between panels.

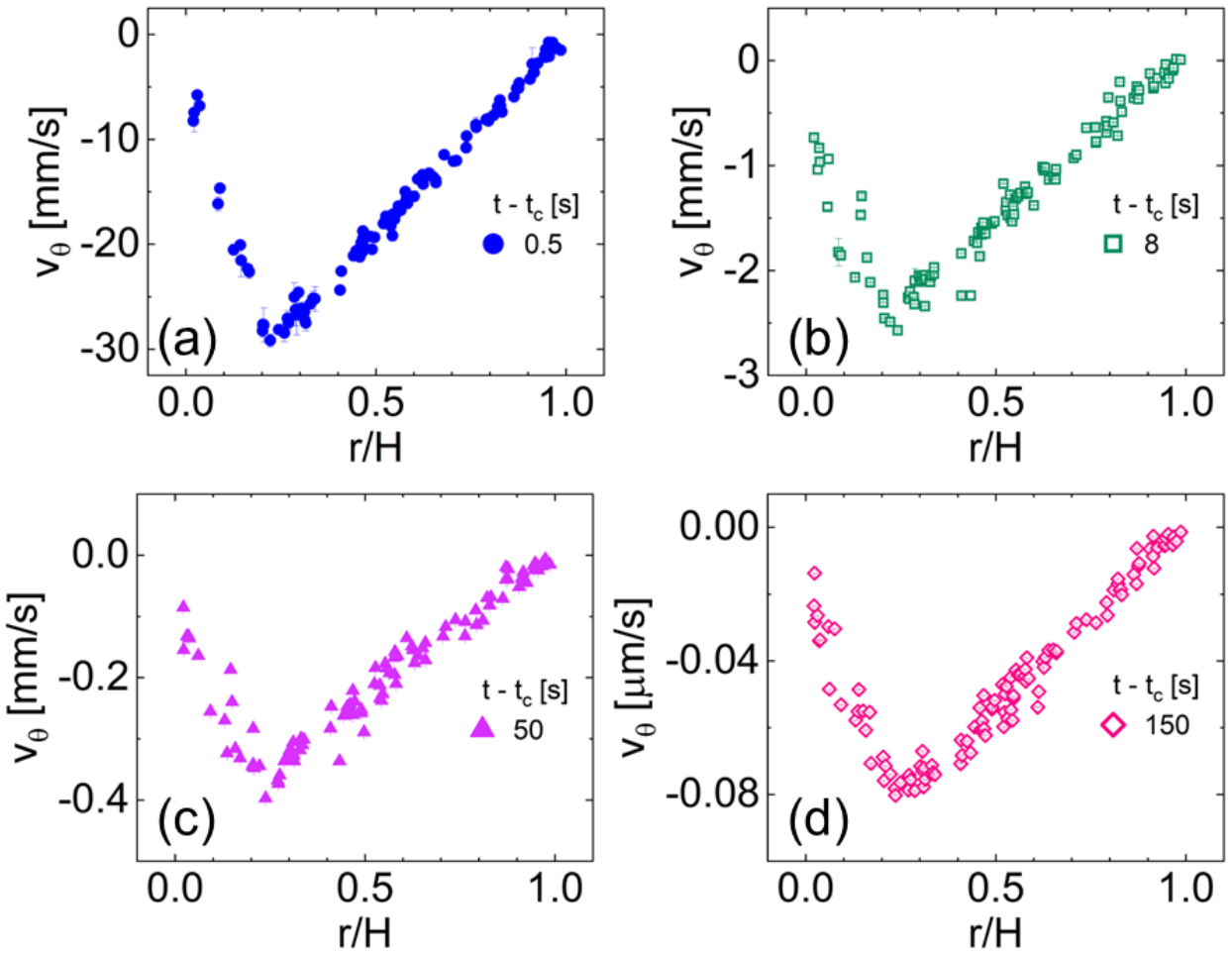

Figure S17: Velocity profiles of P234-NaCl after $t_c = 2150$ s of shear startup flow at $\dot{\gamma} = 0.5$ s^{-1}. These velocity profiles are plotted together in Figure 5g in the main text. Note the y-axis scale may differ between panels.

SI.8 Shear stress fits

The decay of the shear stress in cessation of flow for both P234-NaF and P234-NaCl was fit with a sum of two exponentials:

$$\sigma = a\exp(-bt) + c\exp(-dt) \tag{SI.8.1}$$

Fits of the shear stress for P234-NaF are shown in Figure S18 and for P234-NaCl in Figure S20. Screenshots of tables of the fit parameters for P234-NaF and P234-NaCl are shown in Figures S19 and S21, respectively. Note for P234-NaF, the parameters are for fits to the normalized stress, σ/σ_c.

SI.8.1 P234-NaF

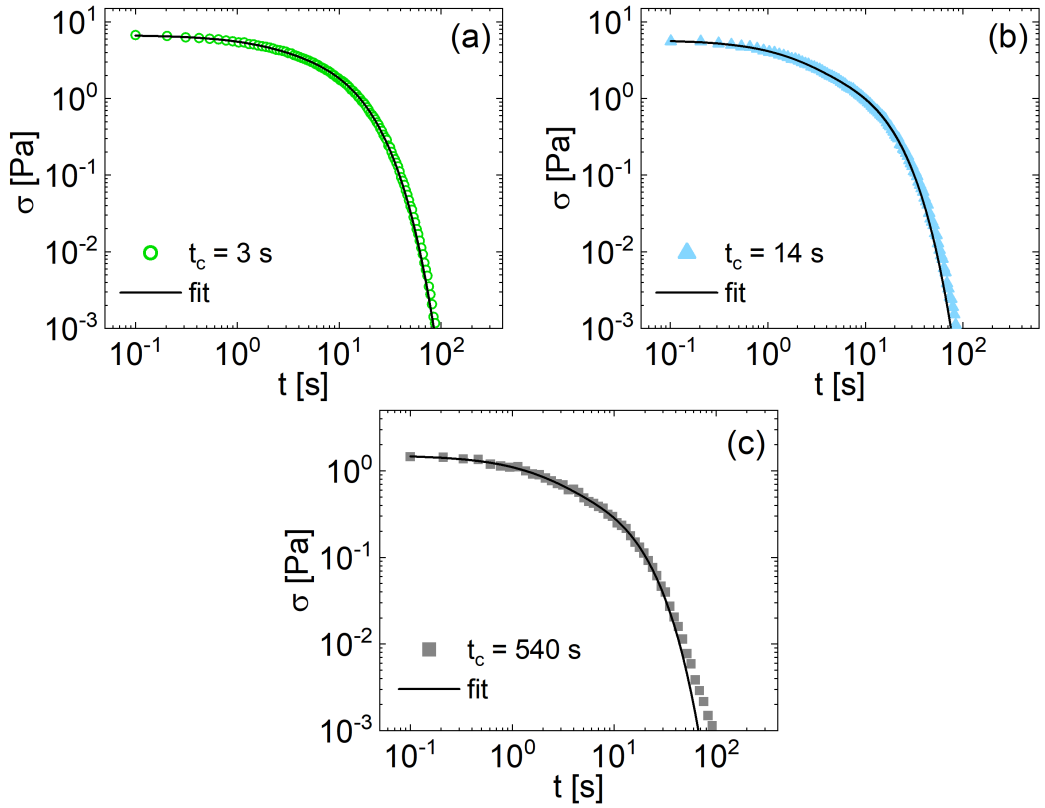

Figure S18: Shear stress fit to a sum of two decaying exponentials for P234-NaF in cessation of flow: t_c = 3 s (a), 14 s (b), and 540 s (c).

$\sigma/\sigma_c = a*\exp(-b*t) + c*\exp(-d*t)$	
tc = 3 s	tc = 14 s
a = 0.2698 (0.2588, 0.2807)	a = 0.5447 (0.5337, 0.5558)
b = 0.5687 (0.533, 0.6045)	b = 0.6205 (0.6002, 0.6408)
c = 0.7368 (0.7248, 0.7488)	c = 0.5022 (0.4901, 0.5143)
d = 0.1003 (0.09889, 0.1018)	d = 0.1056 (0.1033, 0.1079)
tc = 540 s	
a = 0.5235 (0.4715, 0.5754)	
b = 0.6096 (0.5178, 0.7014)	
c = 0.5241 (0.4677, 0.5805)	
d = 0.09916 (0.08884, 0.1095)	

Figure S19: Fitting function and fit parameters for the shear stress fit to a sum of decaying exponentials in cessation of flow of P234-NaF. Fit parameters are shown for each trial: $t_c = 3$ s, 14 s, and 540 s.

SI.8.2 P234-NaCl

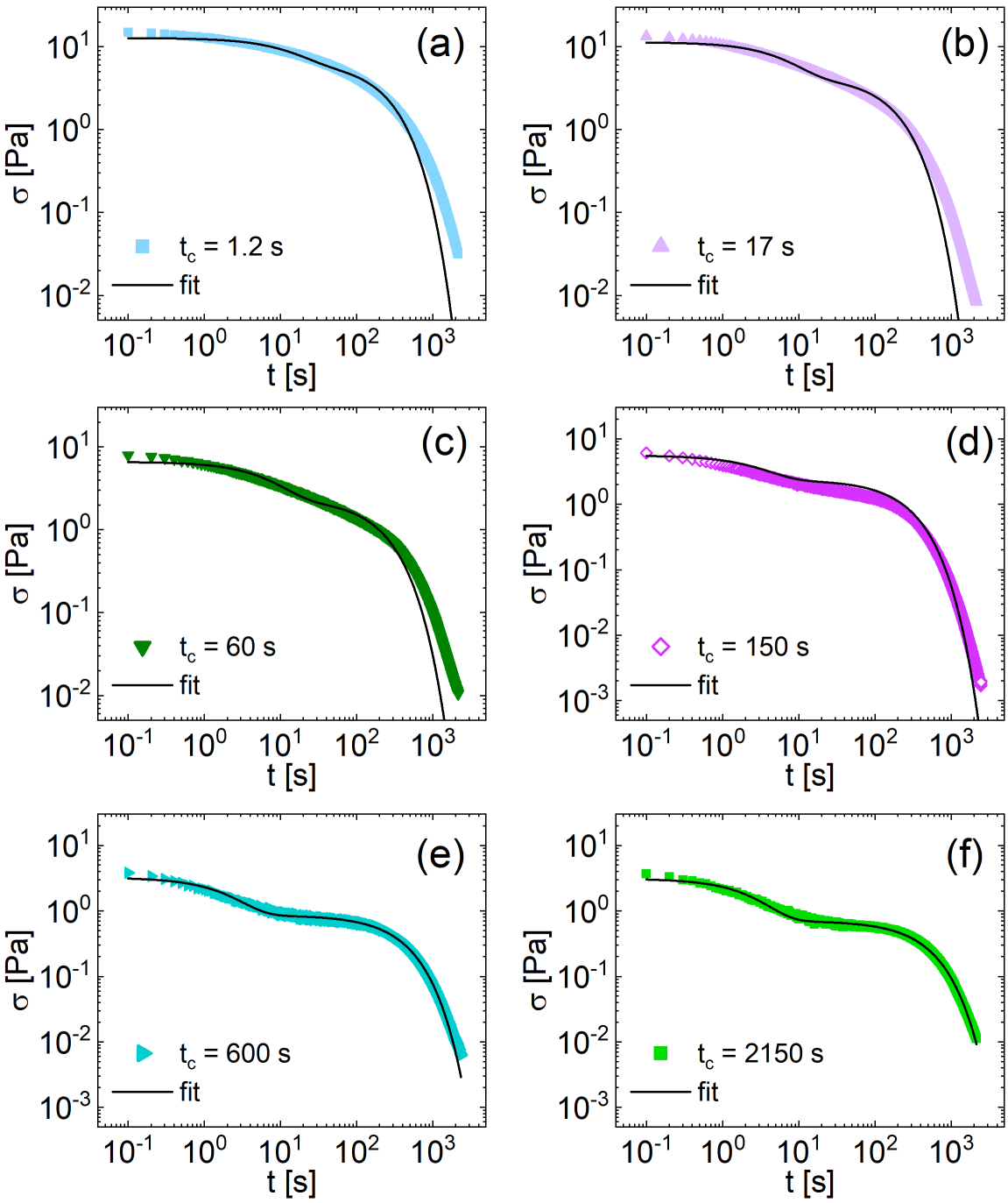

Figure S20: Shear stress fit to a sum of two decaying exponentials for P234-NaCl in cessation of flow: $t_c = 1.2$ s (a), 17 s (b), 60 s (c), 150 s (d), 600 s (e) and 2150 s (f). The fits become better as the time before cessation t_c increases. This behavior potentially indicates that aging effects, which are most substantial at earlier times, impact the stress relaxation.

$\sigma = a*\exp(b*t) + c*\exp(d*t)$	
tc = 1.2 s	tc = 150 s
a = 6.295 (6.195, 6.396)	a = 3.199 (3.152, 3.247)
b = -0.06963 (-0.07209, -0.06717)	b = -0.3254 (-0.3331, -0.3176)
c = 6.491 (6.415, 6.567)	c = 1.812 (1.803, 1.822)
d = -0.004028 (-0.004104, -0.003951)	d = -0.003723 (-0.003766, -0.003679)
tc = 17 s	tc = 600 s
a = 7.015 (6.902, 7.129)	a = 2.374 (2.336, 2.411)
b = -0.1459 (-0.1507, -0.1411)	b = -0.4898 (-0.5014, -0.4783)
c = 4.346 (4.29, 4.402)	c = 0.8565 (0.8518, 0.8613)
d = -0.005428 (-0.005556, -0.0053)	d = -0.002422 (-0.002457, -0.002387)
tc = 60 s	tc = 2150 s
a = 4.26 (4.189, 4.33)	a = 2.403 (2.366, 2.441)
b = -0.133 (-0.1373, -0.1286)	b = -0.3967 (0.387, 0.4064)
c = 2.346 (2.313, 2.379)	c = 0.7036 (0.6977, 0.7094)
d = -0.004344 (-0.004462, -0.004227)	d = -0.002013 (0.001967, 0.002059)

Figure S21: Fitting function and fit parameters for the shear stress fit to a sum of decaying exponentials in cessation of flow of P234-NaCl. Fit parameters are shown for each trial: $t_c = 1.2$ s, 17 s, 60 s, 150 s, 600 s, and 2150 s.

SI.9 Supplementary cessation of flow measurements for P234-NaCl

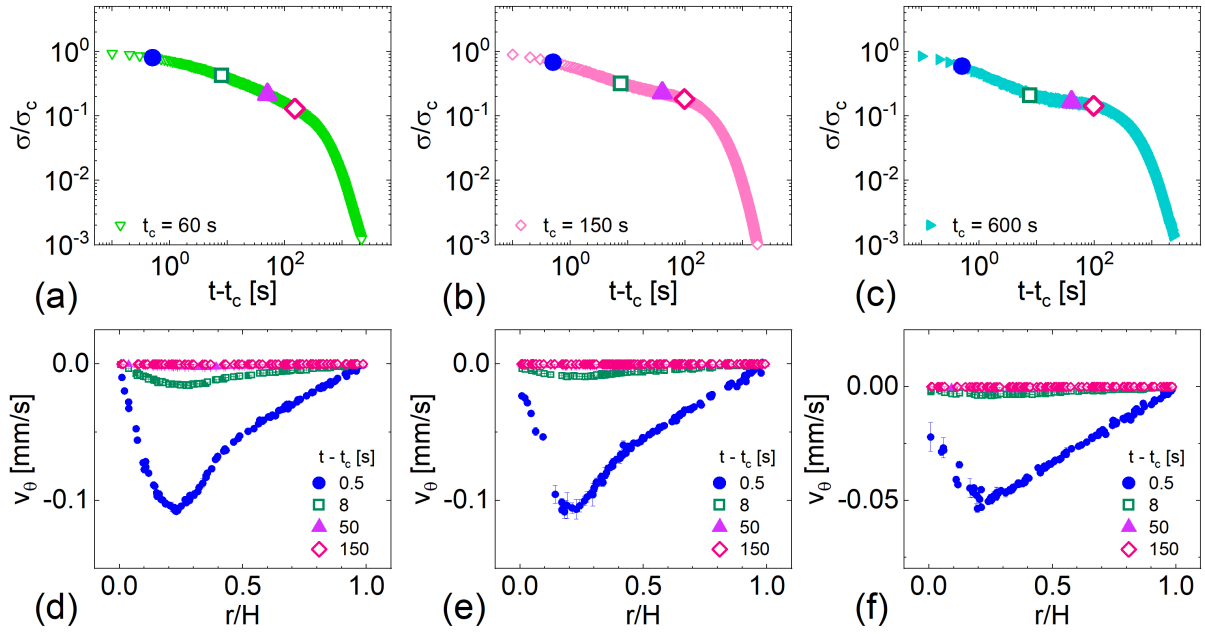

Figure S22: Shear stress (a-c) of P234-NaCl in cessation of flow started after $t_c = 60$, 150, and 600 seconds of startup flow at $\dot{\gamma} = 0.5$ s^{-1}. The corresponding velocity profiles for each shear startup are shown the panel below (d-f). The shear stress is normalized by the final shear stress measured in shear startup, σ_c (Startups shown in Figure S7). Representative velocity profiles (d-f) are shown at four times during the cessation of flow. Velocity profiles are plotted individually in Section SI.7.2.

SI.10 Additional GCB model data

Similar to the results for two adjacent UCM fluids, heterogeneity in the distribution of species A and B across the gap causes fluid retraction in cessation of flow; however here, fluid retraction practically ceases well before the shear stress fully relaxes (Fig. 9a-c vs. d-f). In cessation of flow performed after shear-banded flow has fully developed ($t_c/\tau_{eff} = 4$ at $Wi = 5$; Fig. S23), the stress relaxes rapidly for a brief period ($t^*/\tau_{eff} < 0.2$) and then slows to a more gradual relaxation rate (Fig. S23a). Substantial fluid retraction is observed only during the initial rapid relaxation period (Fig. S23b). Two discrete populations are still present when retraction has essentially stopped (Fig. S23c, t^*/τ_{eff} = 0.2), but the shear stress held by species B has decayed to practically zero by this time (Fig. S23d, t^*/τ_{eff} = 0.2). Therefore, the vast majority of the shear stress is held only by species A beyond this time, and the difference in relaxation rate will not be substantial enough to cause noticeable retraction. Consequently, the timescale for retraction coincides with the timescale for the excess shear stress held by species B to dissipate.

After the excess shear stress held by species B is dissipated, a very minor amount of fluid retraction accompanies the remaining stress relaxation due to the slight shear stress gradient of the concentric cylinder flow geometry. To help visualize this small degree of retraction, the minimum velocity at any time during retraction, v_{min} (e.g. apex of the velocity profiles in Fig. 9d-f), is compared for each stop time t_c/τ_{eff} after shear startups ($Wi = 5$) (Fig. S24). The initial velocity in cessation of flow is an order of magnitude slower when the initial fluid microstructure is approximately homogeneous (Fig. S24, $t_c/\tau_{eff} = 0.2$, 0.45) compared to when the fluid microstructure is significantly heterogeneous (Fig. S24, $t_c/\tau_{eff} = 0.6$, 0.75 and 4), and the decay rate differs greatly. When the starting fluid microstructure is heterogeneous, the retraction speed decelerates much faster than when the microstructure is more homogeneous. At long times when the distribution of species and shear stress held by each component homogenizes, the fluid retraction speed decays at roughly the same rate for all trials, with a time constant roughly equal to the effective relaxation rate τ_{eff}.

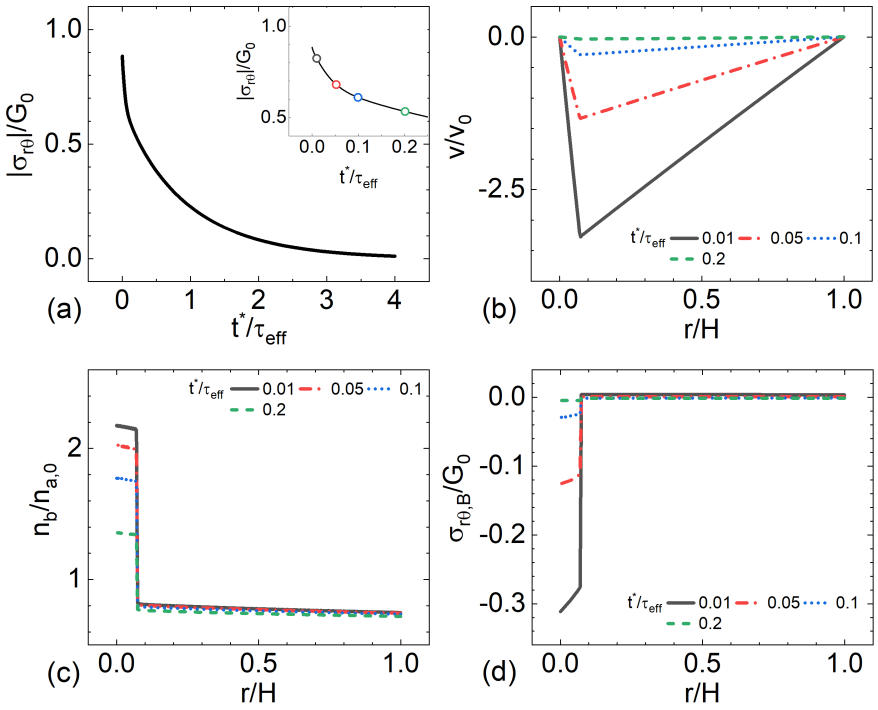

Figure S23: Cessation of flow after shear startup ($t_c = 4\tau_{eff}$) at $Wi = 5$. (a) Shear stress evolution at the inner cylinder ($r/H = 0$). Normalized velocity (b), normalized number density of species B (c), and normalized shear stress of species B as a function of r/H (d) at four times during the stress relaxation (denoted by $\circ$, inset of (a)). Shear stresses are normalized by the elastic modulus at rest, G_0, the velocity is normalized by the imposed wall velocity v_0, and the number densities of species B are normalized by the number density of species A at rest, $n_{A,0}$.

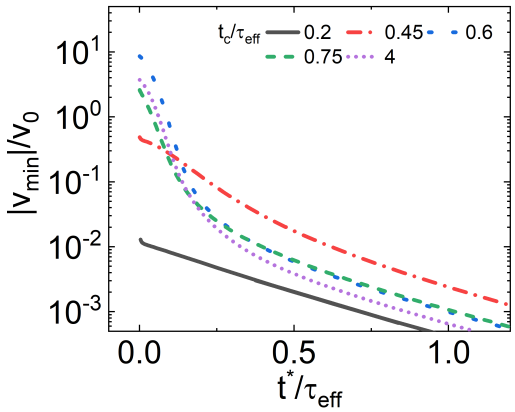

Figure S24: Evolution of v_{min} in cessation of flow started after startup at $Wi = 5$ stopped at five times t_c/τ_{eff}. Velocity is normalized by the imposed wall velocity v_0 for easier comparison.

SI.11 Decay of visible light scattering in P234-NaF

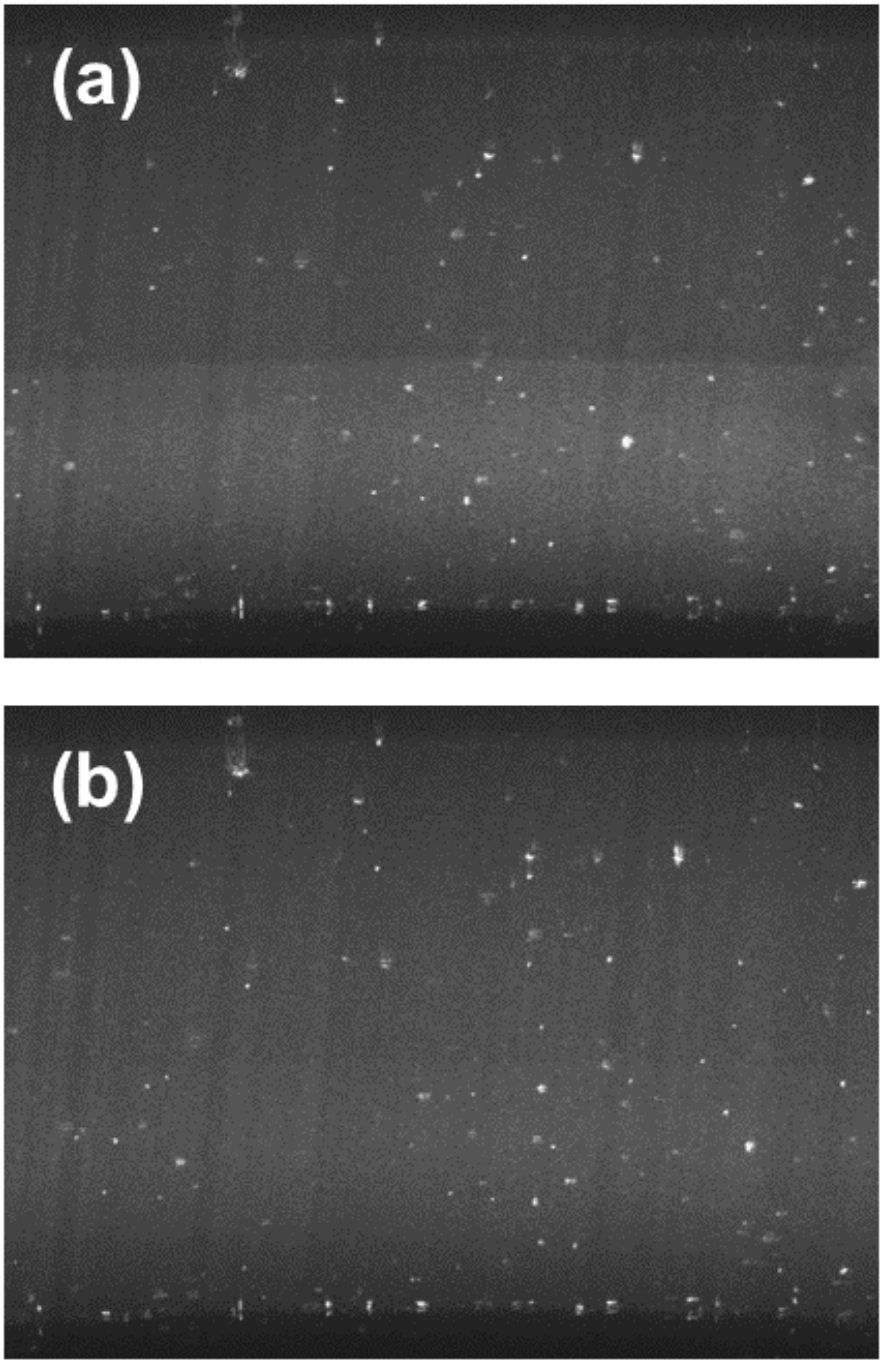

Figure S25: Rheo-PTV images collected (a) $t - t_c = 0$ and (b) $t - t_c = 3$ seconds after the start of cessation of flow for $t_c = 540$ s. Light scattered from the high-shear-rate band of fluid is significantly greater than the low-shear-rate band at the beginning of cessation, but this difference dissipates in a few seconds, a rate consistent with the fast relaxation process measured from fits to the particle trajectories and shear stress.

References

[1] N. Germann, L. Cook, and A. Beris, "Investigation of the inhomogeneous shear flow of a wormlike micellar solution using a thermodynamically consistent model," *J. Non-Newtonian Fluid Mech.*, vol. 207, pp. 21–31, 2014.

[2] P. J. McCauley, M. A. Calabrese, and S. Kumar, "Interplay of wall slip and shear banding in wormlike micelle solutions," *J. Non-Newtonian Fluid Mech.*, vol. 1, no. 1, pp. 1–2, 2023.

[3] N. Germann, L. Cook, and A. N. Beris, "Nonequilibrium thermodynamic modeling of the structure and rheology of concentrated wormlike micellar solutions," *J. Non-Newtonian Fluid Mech.*, vol. 196, pp. 51–57, 2013.

[4] C. Canuto, M. Y. Hussaini, A. Quarteroni, and T. A. Zang, *Spectral methods: fundamentals in single domains*. Springer Science & Business Media, 2007.

[5] R. Peyret, *Spectral methods for incompressible viscous flow*, vol. 148. Springer Science & Business Media, 2002.

[6] L. F. Shampine and M. W. Reichelt, "The MATLAB ODE suite," *SIAM J. Sci. Comput.*, vol. 18, no. 1, pp. 1–22, 1997.

[7] P. J. McCauley, C. Huang, L. Porcar, S. Kumar, and M. A. Calabrese, "Evolution of flow reversal and flow heterogeneities in high elasticity wormlike micelles (WLMs) with a yield stress," *J. Rheol.*, vol. 67, no. 3, pp. 661–681, 2023.

[8] N. Spenley, M. Cates, and T. McLeish, "Nonlinear rheology of wormlike micelles," *Phys. Rev. Lett.*, vol. 71, no. 6, p. 939, 1993.

[9] P. J. McCauley, *Understanding self-assembly and flow heterogeneities in poloxamer wormlike micelles*, ch. Rheo-particle tracking velocimetry analysis development, pp. 57–75. University of Minnesota, 2023.